nanomaterials

MDPI

Article

Coke-Resistant Ni/$CeZrO_2$ Catalysts for Dry Reforming of Methane to Produce Hydrogen-Rich Syngas

Intan Clarissa Sophiana [1,2], Ferry Iskandar [2,3], Hary Devianto [1], Norikazu Nishiyama [4] and Yogi Wibisono Budhi [1,2,*]

[1] Department of Chemical Engineering, Faculty of Industrial Technology, Institut Teknologi Bandung, Bandung 40132, Indonesia; intanclarissas@gmail.com (I.C.S.); hardev@che.itb.ac.id (H.D.)
[2] Research Center for Nanoscience and Nanotechnology, Institut Teknologi Bandung, Bandung 40132, Indonesia
[3] Department of Physics, Faculty of Mathematics and Natural Science, Institut Teknologi Bandung, Bandung 40132, Indonesia; ferry@fi.itb.ac.id
[4] Department of Chemical Engineering, Engineering Science School, Osaka University, Osaka 565-0871, Japan; nisiyama@cheng.es.osaka-u.ac.jp
* Correspondence: y.wibisono@che.itb.ac.id

Abstract: Dry reforming of methane was studied over high-ratio zirconia in ceria-zirconia-mixed oxide-supported Ni catalysts. The catalyst was synthesized using co-precipitation and impregnation methods. The effects of the catalyst support and Ni composition on the physicochemical characteristics and performance of the catalysts were investigated. Characterization of the physicochemical properties was conducted using X-ray diffraction (XRD), N_2-physisorption, H_2-TPR, and CO_2-TPD. The results of the activity and stability evaluations of the synthesized catalysts over a period of 240 min at a temperature of 700 °C, atmospheric pressure, and WHSV of 60,000 mL g^{-1} h^{-1} showed that the 10%Ni/$CeZrO_2$ catalyst exhibited the highest catalytic performance, with conversions of CH_4 and CO_2 up to 74% and 55%, respectively, being reached. The H_2/CO ratio in the product was 1.4, which is higher than the stoichiometric ratio of 1, indicating a higher formation of H_2. The spent catalysts showed minimal carbon deposition based on the thermo-gravimetry analysis, which was <0.01 gC/gcat, so carbon deposition could be neglected.

Keywords: nickel; ceria-zirconia; coke-resistant catalysts; dry reforming of methane; greenhouse gases; syngas production

Citation: Sophiana, I.C.; Iskandar, F.; Devianto, H.; Nishiyama, N.; Budhi, Y.W. Coke-Resistant Ni/$CeZrO_2$ Catalysts for Dry Reforming of Methane to Produce Hydrogen-Rich Syngas. *Nanomaterials* **2022**, *12*, 1556. https://doi.org/10.3390/nano12091556

Academic Editors: Vincenzo Vaiano, Olga Sacco and Narcís Homs

Received: 12 March 2022
Accepted: 27 April 2022
Published: 4 May 2022

1. Introduction

In recent decades, the abundances of methane (CH_4) and carbon dioxide (CO_2) in natural gas reserves and the atmosphere have attracted the attention of researchers for use in the production of value-added products, which would reduce global warming by mitigating the emission of these greenhouse gases [1]. Natural gas utilization often involves reforming technology that converts natural gas into synthesis gas (also known as "syngas"). Reforming technologies include steam, partial oxidative, and dry reforming [2,3]. Steam reforming involves the reaction of CH_4 and steamed water (H_2O), whereas partial oxidative reforming involves the reaction of CH_4 and oxygen (O_2), where the moles of O_2 required are less than the stoichiometric value [4,5]. Dry reforming of methane (DRM) involves the reaction of the greenhouse gases CH_4 and CO_2 to produce syngas containing hydrogen (H_2) and carbon monoxide (CO) at a H_2/CO ratio of approximately 1 [6–9]. The syngas produced in the DRM can be used as a starting material for the manufacture of dimethyl ether, acetic acid, and alcohols via the synthesis of oxo-alcohols as an intermediate or final product in the petrochemical industry [10,11].

The DRM is reversible and endothermic; therefore, a large amount of energy is required to make the process feasible [12]. The DRM requires a catalyst that plays a role

in maximizing the production of syngas by increasing the rate of chemical reactions [13]. During the DRM, a reverse water–gas shift reaction (WGSR) occurs, which produces water (H_2O) to encourage the endothermic steam reforming of methane (SRM) and exothermic steam/carbon gasification as a side reaction. In addition, other side reactions can occur during the DRM: The CO produced via DRM, reverse WGSR, and steam/carbon gasification can encourage the Boudouard reaction, while the CH_4 in the feed can decompose into carbon and H_2. The Boudouard reaction and methane decomposition produce solid carbon, which can cover the active sites on the surface of the catalyst, resulting in catalyst deactivation. The chemical reactions that can occur during the DRM are shown in Equations (1)–(6) below [14].

DRM reaction:

$$CH_4 + CO_2 \rightleftarrows 2CO + 2H_2 \ \Delta H^\circ_{298\ K} = +247\ kJ/mol \quad (1)$$

Reverse WGSR:

$$CO_2 + H_2 \rightleftarrows CO + H_2O \ \Delta H^\circ_{298\ K} = +41\ kJ/mol \quad (2)$$

SRM reaction:

$$CH_4 + H_2O \rightleftarrows CO + 3H_2 \ \Delta H^\circ_{298\ K} = +206\ kJ/mol \quad (3)$$

Boudouard reaction:

$$2CO \rightleftarrows C_{(s)} + CO_2 \ \Delta H^\circ_{298\ K} = -172\ kJ/mol \quad (4)$$

Methane decomposition reaction:

$$CH_4 \rightleftarrows C_{(s)} + 2H_2 \ \Delta H^\circ_{298\ K} = +74\ kJ/mol \quad (5)$$

Steam/carbon gasification reaction:

$$C_{(s)} + H_2O \rightleftarrows CO + H_2 \ \Delta H^\circ_{298\ K} = +131\ kJ/mol \quad (6)$$

Precious metal-based catalysts, such as Pt, Rh, Ru, Pd, and Ir, exhibit high catalytic performance in the DRM and high resistance to carbon deposition on the catalyst surface [15–25]. However, owing to the lack of precious metal resources and high prices, many researchers are focusing on transition metals, such as Ni and Co, which have lower prices [26–36]. Based on the catalytic activity of transition-metal-based catalysts in the DRM, Ni is the only transition metal that is comparable with noble metals [4].

Although Ni-based catalysts have high catalytic activity, these can undergo catalyst deactivation during the DRM via two mechanisms: (1) Carbon deposition that occurs within the temperature range of 500–700 °C, resulting in the blockage of surface active sites, and (2) sintering that occurs within the temperature range of 700–800 °C, which results in a loss of active surface area [31]. The lack of stability of Ni-based catalysts in the DRM may limit their commercial use; therefore, Ni-based catalysts must be modified to improve their catalytic performance and resistance to carbon deposition [4].

The support and promoter materials used in DRM catalysts generally have a high oxygen storage capacity (OSC), which when combined with the active sites of the catalyst, can increase the mobility of oxygen atoms through the crystal lattice and promote the formation of oxygen site vacancies in the catalyst [37]. Several promoters, such as ceria (CeO_2), have been added to conventional Ni/Al_2O_3 catalysts to increase their reduction/oxidation (redox) potential [38,39]. As a result, adding a promoter to conventional catalysts can increase catalytic performance in the DRM [40]. Therefore, the addition of CeO_2, which has a high OSC, to the DRM catalyst on various supports, such as alumina, silica, and zirconia, can improve the catalytic performance.

The use of a catalyst support with weak Lewis acid sites and/or the presence of alkaline sites can improve the performance, stability and coke-resistance of the DRM catalyst, of which the ZrO_2 support fits these criteria [41]. Several researchers have used CeZr as a catalyst support for the DRM [42–49]. Kambolis et al. [48] showed that the use of a ceria-zirconia catalyst support with a high zirconia content (28 wt.% ceria and 72 wt.% zirconia) resulted in high product yields. To date, research using ceria-zirconia-supported Ni catalysts with a high zirconia:ceria ratio and varying Ni contents has not been reported; therefore, it has the potential to be investigated to obtain the optimum catalyst for the DRM.

2. Materials and Methods

2.1. Materials

Cerium(III) nitrate hexahydrate ($Ce(NO_3)_3{\cdot}6H_2O$, >99.99%), zirconium(IV) chloride ($ZrCl_4$, >98%), nickel(II) nitrate hexahydrate ($Ni(NO_3)_2{\cdot}6H_2O$, >99%), and ammonium hydroxide solution (NH_4OH, 25 wt.%) were used in this study and purchased from Merck (Damstadt, Germany). Demineralized water was used throughout the synthesis process. A mixture of CH_4 and CO_2 (50%:50%) was used for the catalyst evaluation experiments. The gases H_2 (99.95%), N_2 (99.99%), and Ar (99.9%) were used as the reducing agent, diluent and inert internal standard for the reaction, and carrier gas for the gas chromatographic (GC) analysis, respectively. All the materials were used without further purification.

2.2. Preparation of Catalysts

2.2.1. Catalyst Based on the ZrO_2 Support

ZrO_2 was prepared via precipitation. $ZrCl_4$ was dissolved in water to form a 0.5 M solution, which was precipitated with a basic solution containing 25 wt.% NH_4OH at pH 9 and a temperature of 60 °C, and then aged by stirring. The precipitate was washed several times using deionized water, dried at 105 °C, and calcined in air at 800 °C for 6 h. An aqueous solution of $Ni(NO_3)_2{\cdot}6H_2O$ and/or $Ce(NO_3)_3{\cdot}6H_2O$ was impregnated into the ZrO_2 support via classical incipient wetness impregnation to form $5\%NiO/ZrO_2$ and $5\%NiO\text{-}10\%CeO_2/ZrO_2$. The resultant samples were dried at 105 °C overnight, and calcined in the air at 700 °C for 6 h.

2.2.2. Catalyst Based on the $Ce_{0.1}Zr_{0.9}O_2$ Support

The $Ce_{0.1}Zr_{0.9}O_2$ mixed metal oxide was prepared via co-precipitation. $Ce(NO_3)_3{\cdot}6H_2O$ and $ZrCl_4$ were dissolved in water to form a 0.5 M solution and co-precipitated with a basic solution containing 25 wt.% NH_4OH at pH 9 and a temperature of 60 °C, and then aged by stirring. The precipitate was washed several times using deionized water, dried at 105 °C for overnight, and calcined in air at 800 °C for 6 h. The $Ce_{0.1}Zr_{0.9}O_2$ ($CeZrO_2$) support was impregnated via classical incipient wetness impregnation with an aqueous solution of $Ni(NO_3)_2{\cdot}6H_2O$, with different amounts of the Ni precursor. The resultant sample was dried at 105 °C overnight and calcined in air at 700 °C for 6 h to finally obtain $5\%NiO/CeZrO_2$ and $10\%NiO/CeZrO_2$.

2.3. Characterization of Catalysts

X-ray diffraction (XRD) was used to determine the crystallinity of the catalysts. XRD measurements on the synthesized catalyst were performed using a Philips X'Pert MDR diffractometer (Royal Dutch Philips Electronics Ltd., Amsterdam, The Netherlands) equipped with a Cu anode tube to produce Cu-Kα (λ = 1.5405 Å) X-rays and operated at 40 kV and 35 mA, using a scan rate of 20° min^{-1}. The catalyst sample was placed in the cell of the diffractometer and irradiated with X-rays. The diffraction data were obtained within a 2θ range of 5–90°, with a scan speed of 4° min^{-1}.

The Brunauer–Emmett–Teller (BET) isotherm method was used to measure the mass-specific surface area of the catalyst sample based on N_2 physisorption using the Micromeritics Tristar II instrument (Micromeritics Instrument Corp., Norcross, GA, USA). The solid powder to be analyzed was placed in the sample cell and weighed. The sample cells were

degassed to remove water molecules and impurity gases adhering to the surface of the catalyst sample. This process was performed at 250 °C for 2 h. After the degassing, the catalyst sample was cooled to room temperature. The sample cells were transferred to the gas sorption analyzer section of the instrument and analyzed. The pore size distribution was determined using the Barrett–Joyner–Halenda (BJH) method.

Hydrogen temperature-programmed reduction (H_2-TPR) was used to determine the interactions between metals. A Micromeritics Chemisorb 1750 instrument (Micromeritics Instrument Corp., Norcross, GA, USA) was used to carry out H_2-TPR analysis. The catalyst (70 mg) was used to fill a U-shaped quartz tube, placed in a furnace, and degassed with Ar at 150 °C for 1 h. Thereafter, the sample was cooled to room temperature, and reduced under a flow rate of 40 mL min^{-1} of 5% H_2 in Ar within the temperature range of 30–900 °C using a heating rate of 10 °C min^{-1}. The TPR profile was recorded using a thermal conductivity detector (TCD), which monitored the consumption of H_2 by the catalyst sample.

Carbon dioxide temperature-programmed desorption (CO_2-TPD) was used to characterize the type of Lewis acid sites on the surface of the catalyst by measuring the number of CO_2 molecules absorbed during heating at a constant temperature. During CO_2-TPD, the sample is heated in an inert gas below a specific temperature, at which point the bond between the adsorbed gas and sample is broken, resulting in desorption of the gas. TPD measurements were carried out in a Micromeritics Chemisorb 2750 unit. The sample (70 mg) was introduced into a U-shaped quartz sample tube for each analysis. The probe gas used in the analysis was 5% CO_2/He. Prior to the measurements, the catalyst sample was purged with He at 200 °C for 1 h to remove weakly bonded species. CO_2 gas adsorption was carried out at 50 °C for 30 min using the 5% CO_2/He gas mixture at a flow rate of 30 mL min^{-1} to ensure that the probe gas molecules saturated all sites on the surface of the catalyst. After adsorption, the sample was purged with He for 30 min. The desorption process was conducted between 50 and 900 °C, with a heating rate of 10 °C min^{-1}. During the TPD stage, the concentration of the desorbed gas was measured using a TCD.

Thermogravimetric analysis (TGA) was used to measure the amount of carbon deposited on the surface (and in the pores) of the catalyst after the DRM. TGA, using the Shimadzu TA-60WS instrument (Shimadzu Corp., Kyoto, Japan), required a sample of approximately 5–10 mg to be placed in a cell and heated under an air-flow (50 mL min^{-1}) from room temperature to 800 °C at a rate of 20 °C min^{-1}.

2.4. Catalytic Performance Evaluation

Catalyst evaluation in the DRM was conducted at atmospheric pressure in a quartz fixed-bed reactor tube (ID = 10 mm) at 700 °C for 240 min. For each test, 60 mg (80–120 mesh) of the catalyst was packed between two ceramic wool plugs to keep the catalyst in a fixed position and diluted with 300 mg of SiC. First, the catalyst was purged with N_2 at 400 °C for 1 h and reduced in a 1:1 H_2:N_2 gas mixture flowed at a rate of 100 mL min^{-1}, while heating at a temperature of 700 °C for 2 h. Then, the system was purged with N_2 at a flow rate of 100 mL min^{-1} for 30 min. The feed gas flow rate used for the activity and stability evaluations was regulated using a mass flow controller. The feed gas used was a mixture of CO_2:CH_4:N_2 at a ratio of 1:1:1. The flow rate of the feed gas mixture was set at 60 mL min^{-1}, resulting in a weight-hourly space velocity (WHSV) of 60,000 mL g^{-1} h^{-1}.

The products and unreacted gas feed were analyzed using online gas chromatography (Shimadzu GC-14B, Shimadzu Corp., Kyoto, Japan), which was carried out every 10 min, with the amount of sample analyzed being ca. 1 mL. After the feed through the reactor under the operating conditions was determined, the product stream from the reactor output was condensed to separate the H_2O content caused by the reverse WGSR using a condenser. As a safety precaution, the H_2O present in the reactor effluent must be condensed before the rest of the gas stream is analyzed in the online GC. The gas chromatograph was equipped with two columns, namely, Porapak-Q (PQ) and Molecular Sieve-5A (MS), arranged in parallel. The Porapak-Q column was used to analyze CO_2, while the MS-5A column was

used to analyze H_2, N_2, CH_4, and CO. The conversion, yield, and H_2/CO ratio were evaluated using Equations (7)–(11).

$$CH_4 \text{ conversion } (\%) = \frac{F_{CH_{4,in}} - F_{CH_{4,out}}}{F_{CH_{4,in}}} \times 100\% \quad (7)$$

$$CO_2 \text{ conversion } (\%) = \frac{F_{CO_{2,\,in}} - F_{CO_{2,\,out}}}{F_{CO_{2,in}}} \times 100\% \quad (8)$$

$$H_2 \text{ yield } (\%) = \frac{F_{H_{2,out}}}{2\,[F_{CH_{4,in}}]} \times 100\% \quad (9)$$

$$CO \text{ yield } (\%) = \frac{F_{CO,\,out}}{F_{CH_{4,in}} + F_{CO_{2,in}}} \times 100\% \quad (10)$$

$$\frac{H_2}{CO} = \frac{F_{H_{2,out}}}{F_{CO,\,out}} \quad (11)$$

where F_{CH_4}, F_{CO_2}, F_{H_2}, and F_{CO} are the flow rates of CH_4, CO_2, H_2, and CO, respectively.

3. Results and Discussion

3.1. Characterization of Catalysts

The ceria-zirconia-supported Ni catalysts prepared in this study were characterized using XRD, N_2 physisorption, H_2-TPR, CO_2-TPD, and TGA.

3.1.1. Crystalline Phase and Catalyst Crystallinity

XRD was used to determine the crystal phases and crystallinities of the catalysts. The XRD diffraction patterns consist of several reflections, with their intensities plotted on the *y*-axis and the measured diffraction angle plotted on the *x*-axis. The results of the XRD analysis for the ZrO_2-supported Ni catalyst are shown in Figure 1. The XRD pattern of the ZrO_2 support shows the crystalline phase of a monoclinic structure (m-ZrO_2) with intense reflections at 2θ = 24.2°, 28.2°, 31.4°, and 34.3° [JCPDS 37-1484]. The obtained diffraction pattern of m-ZrO_2 is similar to that of Basahel et al. [50] and Sophiana et al. [51].

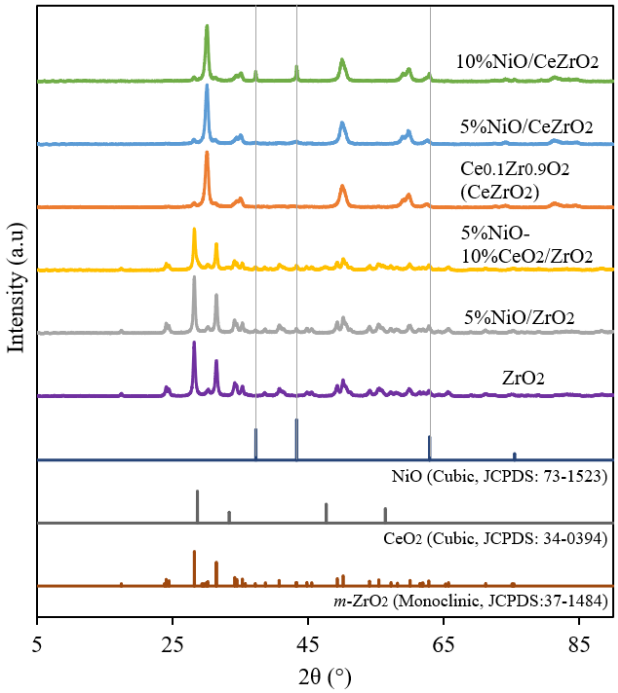

Figure 1. XRD pattern on a ceria-zirconia-supported nickel catalyst.

Meanwhile, the XRD pattern of the mixed metal oxide $Ce_{0.1}Zr_{0.9}O_2$ support is similar to that of the cubic fluorite structure of CeO_2, without additional reflections corresponding to ZrO_2 being observed with intense reflections at 2θ = 30.1°, 50.1°, and 60.1°. This indicates the incorporation of ZrO_2 into the CeO_2 lattice, leading to the formation of a solid solution, while maintaining the fluorite structure. The diffraction pattern of $Ce_{0.1}Zr_{0.9}O_2$ is similar to that reported by Wolfbeisser et al. [43], Deng et al. [52], and Pham et al. [53].

As shown in Figure 1, the Ni formed in the catalyst is in the form of NiO. The three prominent reflections of NiO are observed at 37.28°, 43.30°, and 62.92°, according to JCPDS 73-1523. The intensities of the NiO reflections in the diffraction pattern of the 10%NiO/$CeZrO_2$ catalyst are higher than those observed in the diffraction patterns of the other catalysts owing to its higher NiO content.

3.1.2. Surface Area and Pore Size Distribution of the Catalysts

The BET method was used to determine the mass-specific surface area of each catalyst, while the BJH method was used to determine the pore size distribution of the catalyst. These methods are based on the amount of N_2 adsorbed and desorbed from the sample. The physical properties of the catalyst in the form of a mass-specific surface area, pore diameter, and pore volume of the synthesized catalyst are listed in Table 1.

Table 1. Physical property of ceria-zirconia-supported nickel catalyst.

Catalyst	Surface Area (m^2 g^{-1})	Pore Diameter (nm)	Total Pore Volume (cm^3 g^{-1})
ZrO_2	29.19	18.54	0.135
5%NiO/ZrO_2	17.23	22.16	0.095
5%NiO-10%CeO_2/ZrO_2	24.62	7.73	0.047
$Ce_{0.1}Zr_{0.9}O_2$ ($CeZrO_2$)	39.83	13.14	0.131
5%NiO/$CeZrO_2$	30.40	14.78	0.112
10%NiO/$CeZrO_2$	28.75	16.10	0.116

It can be observed that the addition of 10 wt.% CeO_2 to ZrO_2 increases the surface area and decreases the pore diameter. The ZrO_2 support has a surface area of 29.19 m^2 g^{-1} and pore diameter of 18.54 nm. Adding 5 wt.% NiO to the ZrO_2 support reduces the surface area to 17.23 m^2 g^{-1} and increases the pore diameter to 22.16 nm. This is due to the addition of NiO, which undergoes sintering and agglomeration during calcination; thus, blocking the pores of the catalyst. Meanwhile, the impregnation of 10 wt.% CeO_2 in 5%NiO/ZrO_2 catalyst increases the surface area above that of 5%NiO/ZrO_2 because 10 wt.% CeO_2 prevents NiO agglomeration in the catalyst.

Adding 10 wt.% CeO_2 to ZrO_2 via co-precipitation to form $Ce_{0.1}Zr_{0.9}O_2$ ($CeZrO_2$) can increase the surface area by approximately 30% to 39.83 m^2 g^{-1} with a pore diameter of 18.54 nm. Addition of 5 wt.% NiO and 10 wt.% NiO to the $CeZrO_2$ support decreases the surface area of the catalyst and increases the pore diameter. As more NiO is impregnated into the support, the surface area of the catalyst decreases, and the pore diameter increases. This is due to the addition of NiO, which undergoes sintering and agglomeration during calcination of 700 °C. Meanwhile, nickel sintering occurs at a temperature of 700 °C [31]. This sintering process can make metal agglomerate and block the catalyst's pores [54].

- Catalyst Surface Area (via the BET Method)

The surface area of the catalyst affects the internal diffusion rate, where the reactants are physically adsorbed through the catalyst pores toward the active center of the catalyst. The adsorption–desorption isotherms of N_2 for the ZrO_2- and $CeZrO_2$-supported NiO catalysts are shown in Figure 2. The isotherms were analyzed using categories created by the International Union of Pure and Applied Chemistry (IUPAC) for the analysis of pores. Based on the plotted results of the volume of N_2 adsorbed and desorbed versus relative pressure, there are six types of isotherm classifications that can be made.

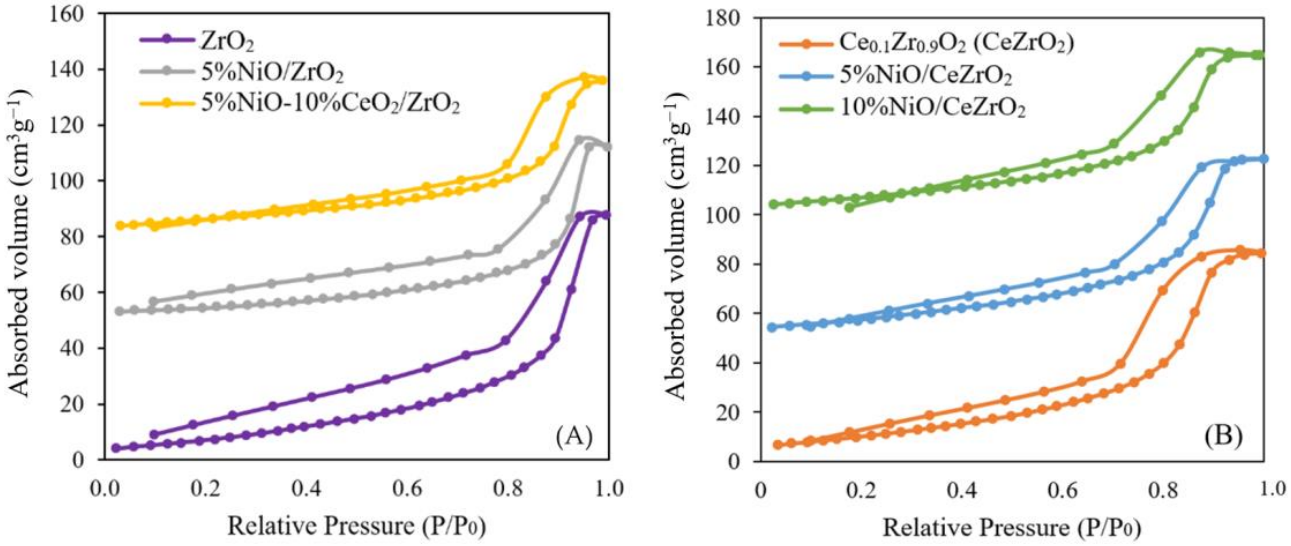

Figure 2. Nitrogen adsorption–desorption of catalyst: (**A**) ZrO_2-supported NiO catalyst and (**B**) $CeZrO_2$-supported NiO catalyst.

In Figure 2A, the NiO catalyst supported on ZrO_2 exhibits a type IV isotherm, corresponding to the classification of mesoporous solids, where this classification describes monolayer-multilayer adsorption on the mesoporous walls. Mesoporous solids have pore diameters in the range of 2–50 nm. In this phenomenon, loop hysteresis occurs because of capillary condensation in the mesopores. In Figure 2B, the isotherm of the $CeZrO_2$-supported NiO catalyst is also type IV. The N_2 physisorption results for the CeZr sample also agreed with the results reported by Deng et al. [52] and Singha et al. [25].

For the NiO catalyst supported by ZrO_2 and $CeZrO_2$, it can be seen that the adsorbed gas at $P/P_0 = 0$ is very small, and the monolayer region is not full. At $P/P_0 < 0.1$, gas adsorption begins to saturate the "monolayer", even though the amount adsorbed is still very small. At $P/P_0 = 0.1$–0.4, multilayer adsorption starts to occur, but the amount of N_2 adsorbed on the $CeZrO_2$-supported catalyst was less than that adsorbed on the ZrO_2-supported catalyst. The type of hysteresis loop observed isa type H_2(b), which does not show limiting adsorption at high P/P_0. Desorption of this isotherm type contains areas associated with hysteresis closure owing to the stress strength.

- Catalyst Pore Size Distribution (via the BJH Method)

The pore size distribution profiles of the ZrO_2- and $CeZrO_2$-supported NiO catalysts under isothermal conditions are shown in Figure 3. Figure 3A shows that the size of the pores in the bare ZrO_2 support range from 2 to 45 nm, with an average pore size of 18.54 nm and a total pore volume of 0.135 $cm^3\ g^{-1}$. The addition of 5wt.% NiO to the ZrO_2 support widens the pore size range when compared with that of the bare ZrO_2, with a larger average pore diameter of 22.16 nm and total pore volume of ca. 0.095 $cm^3\ g^{-1}$ being obtained for the supported catalyst. This larger pore size is probably caused by the calcination carried out twice, which causes NiO and ZrO_2 to agglomerate and aggregate. Meanwhile, CeO_2 impregnation in the 5%NiO/ZrO_2 catalyst results in a narrow pore size distribution, with a smaller average pore size of 7.73 nm and total pore volume of ca. 0.047 $cm^3\ g^{-1}$. This is due to the presence of a CeO_2 component that fills the pores of the ZrO_2 support, resulting in a decrease in the pore diameter and volume of the catalyst.

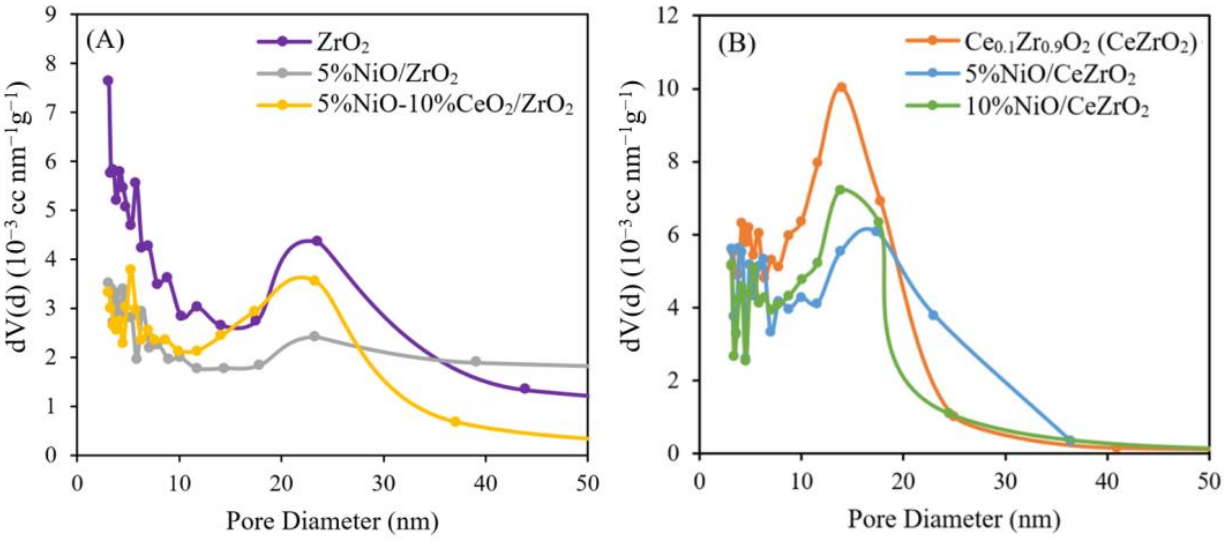

Figure 3. Pore distribution of catalyst: (**A**) ZrO_2-supported NiO catalyst and (**B**) $CeZrO_2$-supported NiO catalyst.

In Figure 3B, it can be seen that the sizes of the pores in the bare $CeZrO_2$ support range from 2 to 30 nm, with an average pore size of 13.14 nm and a total pore volume of 0.131 $cm^3\ g^{-1}$. The addition of 5 wt.% NiO to $CeZrO_2$ support results in a narrower pore size distribution range than that of the bare $CeZrO_2$, with an average pore diameter of 14.78 nm and a total pore volume of 0.112 $cm^3\ g^{-1}$. Meanwhile, the addition of 10 wt.% NiO to the $CeZrO_2$ support had a more comprehensive pore distribution range than the bare $CeZrO_2$, with an average pore diameter of 16.10 nm and a total pore volume of 0.116 $cm^3\ g^{-1}$. This larger pore size is probably caused by the calcination being carried out twice, which causes NiO and $CeZrO_2$ to agglomerate.

3.1.3. Catalyst Reducibility

H_2-TPR was performed to determine the level of reduction (i.e., reducibility) of the catalyst and the ability of H_2 to diffuse into the catalyst. The H_2-TPR study is important because it informs on how to carry out the activation of the catalyst prior to the catalyst performance evaluation since the synthesized catalyst is in the metal oxide form, whereas the active phase required for the DRM is metallic Ni (Ni^0). Catalyst reduction using H_2 produces H_2O as the main gaseous product. The H_2-TPR results for the catalysts show that H_2 consumption occurs at temperatures between 200 and 840 °C. The H_2-TPR profiles of the NiO catalysts supported on ZrO_2 and $CeZrO_2$ are shown in Figure 4.

The reduction initiation temperatures of the ZrO_2, 5%Ni/ZrO_2, and 5%Ni-10%CeO_2/ZrO_2 samples are approximately 217, 238, and 200 °C, respectively. Meanwhile, the reduction initiation temperatures of the $CeZrO_2$, 5%Ni/$CeZrO_2$, and 10%Ni/$CeZrO_2$ samples are approximately 250, 209, and 215 °C, respectively. The Ni catalyst exhibits a first reduction peak at approximately 400 °C, which indicates the reduction of NiO to Ni^0. The second peak in the H_2-TPR profile of the $CeZrO_2$-supported Ni catalyst indicates the reduction of CeO_2. The addition of CeO_2 to ZrO_2 to form $CeZrO_2$ can increase the OSC and redox properties of the mixed metal oxide. Among the synthesized catalysts, the 10%Ni/$CeZrO_2$ catalyst has the most intense peak for Ni reduction at a low temperature (399 °C). This is due to the higher amount of NiO and shift of the reduction peak to a lower temperature caused by the spillover effect of H_2. This good redox properties of the $CeZrO_2$ support allow for a more effective transfer of oxygen species [42].

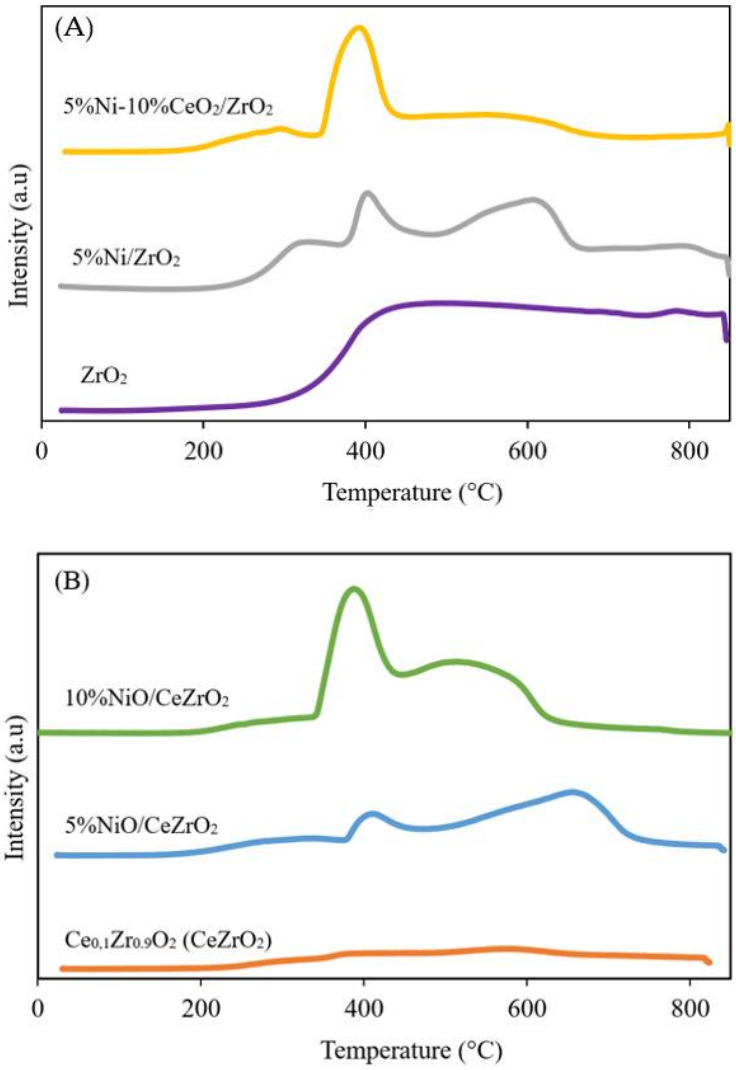

Figure 4. H_2-TPR profiles of catalyst: (**A**) ZrO_2-supported Ni catalyst and (**B**) $CeZrO_2$-supported Ni catalyst.

3.1.4. Basicity of the Catalysts

The chemical nature of the catalyst can affect its performance in the DRM. Catalysts with strong Lewis basic sites can facilitate the adsorption of acidic CO_2 molecules and assist in carbon gasification to prevent carbon deposition during the DRM [38]. Meanwhile, a catalyst with strong Lewis acid sites can direct the reaction toward carbon deposition [55].

CO_2-TPD was performed to determine the basicity of each catalyst by measuring the number of absorbed CO_2 molecules on the surface. If CO_2 is mostly desorbed at high temperatures, then the basicity of the catalyst is high because CO_2 is an acidic probe. However, if CO_2 is desorbed at low temperatures, then the basicity of the catalyst is low. The desorption of CO_2 from the catalyst can be divided into three parts: At temperatures between 100 and 200 °C (first section), 250 and 420 °C (second section), as well as 580 and 760 °C (third section), indicating weak, medium, and strong basic sites on the surface of the DRM catalyst. The desorption peak of the catalyst, indicating weak basic sites, is related to the adsorption of CO_2 by Lewis acid-base pairs [56]. The results of CO_2-TPD for the ZrO_2- and $CeZrO_2$-supported NiO catalysts are shown in Figure 5.

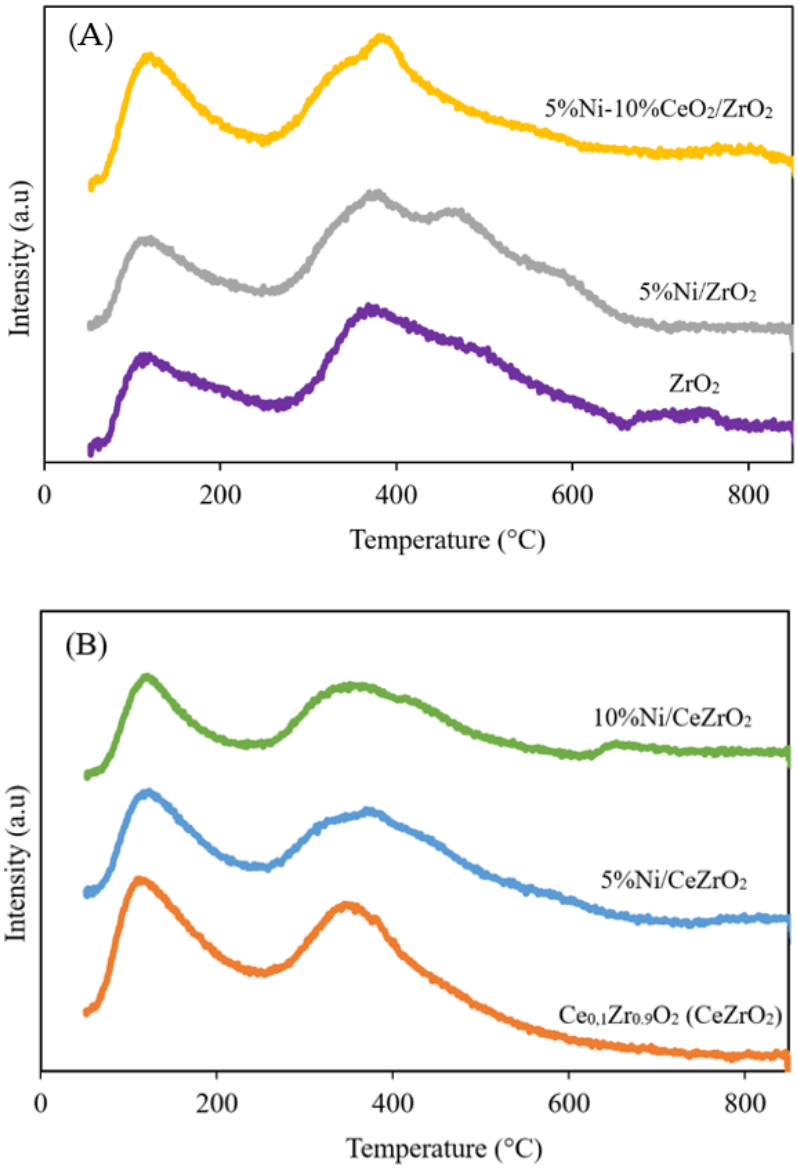

Figure 5. CO_2-TPD profiles of catalyst: (**A**) ZrO2-supported Ni catalyst and (**B**) CeZrO2-supported Ni catalyst.

Figure 5A shows the CO_2 desorption profile of the ZrO_2-supported NiO catalyst. Desorption of CO_2 on the bare ZrO_2 support shows that desorption occurs in the first and second sections, indicating the presence of weak and moderate alkaline sites, respectively, where the desorption peaks at moderate temperatures are more intense, implying that the catalyst had a higher number of moderate alkaline sites than weak basic sites. The catalyst with the addition of 5 wt.% NiO gave results that are not too different from those of the bare ZrO_2 support, where desorption occurs in the first and second sections, indicating the presence of weak and moderate alkaline sites, where the desorption peak at the medium temperatures is more intense, implying that these sites are dominant on the catalyst surface. Meanwhile, the presence of 10 wt.% CeO_2 in the 5%NiO/ZrO_2 catalyst gave different results, where the desorption peaks at the low and medium temperatures are almost the same, indicating that neither the weak or moderate base sites are dominant.

Figure 5B shows the desorption profile of CO_2 from the NiO catalyst supported on $CeZrO_2$. Desorption of CO_2 on the bare $CeZrO_2$ support shows that desorption occurs in the first and second sections, indicating weak and moderate alkaline sites, where the desorption peaks at low temperatures were more intense, implying that this catalyst has a

higher number of weak basic sites than moderate basic sites. Catalysts with the addition of 5 wt.% and 10 wt.% NiO show results that are similar to those of the $CeZrO_2$ support, where the desorption peak at a moderate temperature is more intense, indicating that this catalyst predominantly has moderately alkaline sites. Overall, the synthesized catalysts show desorption in the first and second sections, indicating the presence of weak and moderate basic sites. The low CO_2 desorption temperature (approximately 99 °C) can be attributed to weakly physisorbed CO_2 [57].

3.2. Activity and Stability of the Catalysts

Catalysts are needed for the DRM to maximize syngas production by increasing the rate of the chemical reaction [13]. At an operating temperature of 700 °C and atmospheric pressure, the maximum equilibrium conversion, product yield, and H_2:CO ratio that can be achieved, according to thermodynamic calculations, were based on the simulation results of Aspen Plus v.10 with the Peng–Robinson equation of state using the RGIBBS reactor model and a CO_2:CH_4 ratio of 1, as well as on the calculation performed by Wang et al. [58]. In this study, commercial catalysts were also evaluated for comparison, in addition to evaluating the performance of the synthesized catalysts. The commercial catalysts used were the methanation (containing 28 wt.% Ni, 60 wt.% Al, and 12 wt.% Ca) and steam reforming catalysts (containing 25 wt.% Ni, 58 wt.% Al, 1 wt.% Si, 14 wt.% Ca, and 1 wt.% K).

Figure 6 shows the conversion profiles of CH_4 and CO_2 for the synthesized and commercial catalysts. The 5%Ni/ZrO_2 catalyst with no added CeO_2 exhibits an average conversion of CH_4 and CO_2 of ca. 58% and 42%, respectively. The impregnation of 10 wt.% CeO_2 into the 5%Ni/ZrO_2 catalyst increases the catalyst activity, with average conversions of CH_4 and CO_2 of ca. 72% and 56%, respectively. The 10%Ni/$CeZrO_2$ catalyst shows higher activity, with average conversions of CH_4 and CO_2 of ca. 74% and 55%, respectively, when compared with the 5%Ni/$CeZrO_2$ catalyst, with an average conversion of CH_4 and CO_2 of ca. 70% and 54%, respectively. This implies that having more Ni in the catalyst improves catalytic performance possibly due to the higher number of active sites per mass of Ni. Meanwhile, the commercial steam reforming catalyst exhibits the highest activity, with average conversions of CH_4 and CO_2 of ca. 85% and 65%, respectively. However, when using the commercial methanation catalyst, the activity decreases significantly at the 40^{th} min of the experiment due to catalyst deactivation via carbon deposition. The average CH_4 and CO_2 conversions during the performance evaluation over 240 min for the commercial methanation catalyst is ca. 23% and 18%, respectively.

Figure 7 shows the H_2 and CO yields for the synthesized and commercial catalysts. The 5%Ni/ZrO_2 catalyst achieves average H_2 and CO yields of ca. 36% and 39%, respectively. The impregnation of 10 wt.% CeO_2 into the 5%Ni/ZrO_2 catalyst increases the yields of H_2 and CO, with averages of ca. 48% and 44%, respectively. The 10%Ni/$CeZrO_2$ catalyst achieves average H_2 and CO yields of ca. 51% and 43%, respectively, when compared with the 5%Ni/$CeZrO_2$ catalyst, with yields of H_2 and CO of ca. 46% and 43%, respectively.

The combination of CeO_2 and ZrO_2 in the CeO_2-ZrO_2 support results in better activity than that of ZrO_2 alone, where the 5%Ni/$CeZrO_2$ catalyst exhibits 20–30% higher activity than the 5%Ni/ZrO_2 catalyst. Meanwhile, the commercial steam reforming catalyst achieves a higher CH_4 conversion than the synthesized catalysts. This is because the number of active Ni sites in the commercial steam reforming catalyst is greater than that in the synthesized catalysts; therefore, more reactants are converted over the commercial steam reforming catalyst. The commercial steam reforming catalyst has an Ni content of 25 wt.%, whereas the synthesized catalysts have an Ni content of 10 wt.%. This is due to the improved oxygen storage and mobility in the $CeZrO_2$ support than in the CeO_2 and ZrO_2 alone [59]. Based on the conversion value of the reactants per mass of active Ni in the catalyst, the 10%Ni/$CeZrO_2$ catalyst has conversion values of CH_4 and CO_2 that are 2.2 and 2.1 times higher than those of commercial steam reforming catalyst.

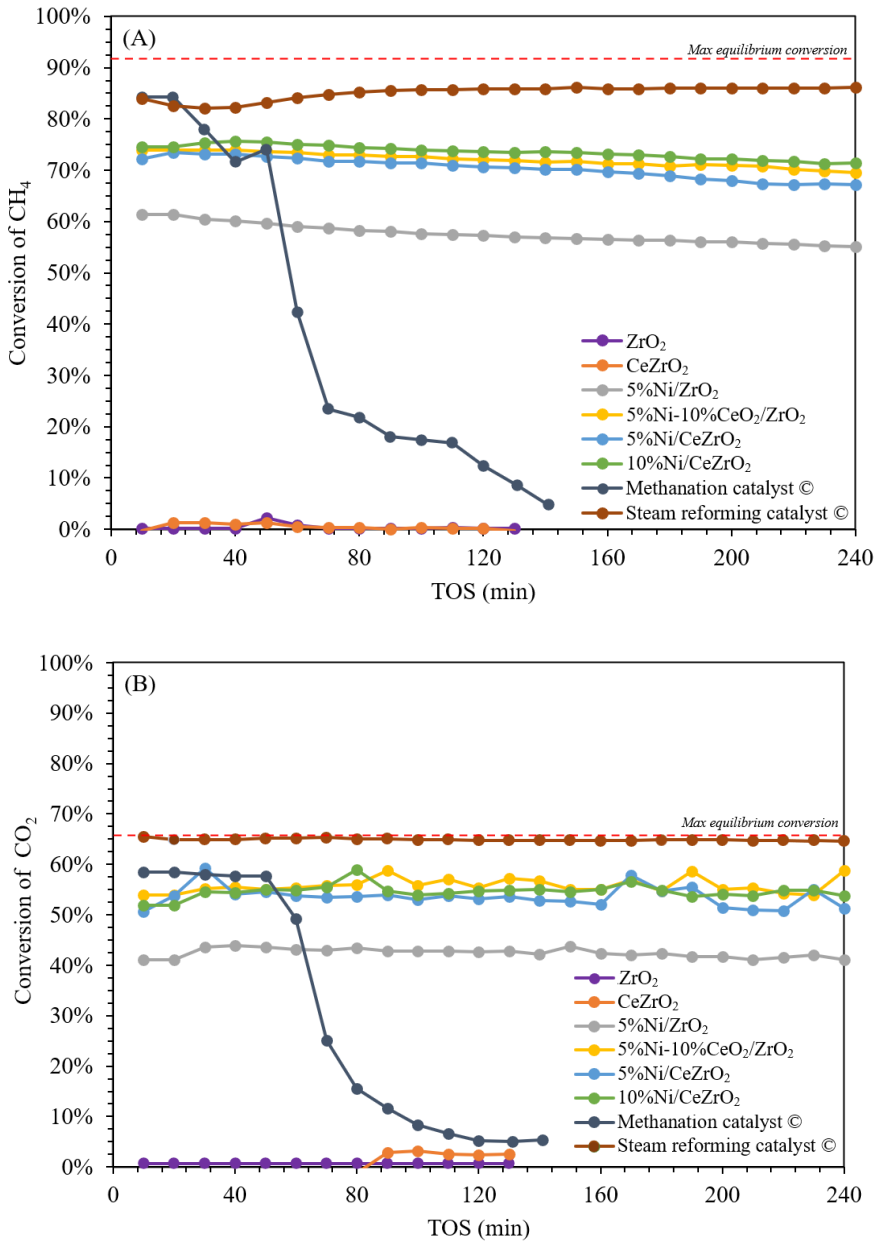

Figure 6. Conversion of reactant on a ceria-zirconia-supported nickel catalyst: (**A**) CH_4 and (**B**) CO_2 (temperature of 700 °C, atmospheric pressure, WHSV 60,000 mL g^{-1} h^{-1}).

For the commercial steam reforming catalyst, the average yields of H_2 and CO products are ca. 66% and 54%, respectively, with the H_2 yields gradually decreasing throughout the duration of the experiment, although the CH_4 conversions are stable. This is due to the side reaction of carbon formation by the decomposition reaction of methane ($CH_4 \rightleftarrows C + 2H_2$), which occurs at temperatures above 640 °C in addition to the DRM [31]. At 700 °C, the formation of carbon occurs more spontaneously via the methane decomposition reaction than via the Boudouard reaction based on the change in the Gibbs free energy (ΔG) of the two reactions. The methane decomposition reaction tends to be more dominant in the steam reforming and methanation catalysts. Meanwhile, the yield of H_2 tends to decrease throughout the duration of the experiment when compared with that of CO. This is due to the reverse WGSR ($CO_2 + H_2 \rightleftarrows CO + H_2O$), which consumes H_2 and forms CO.

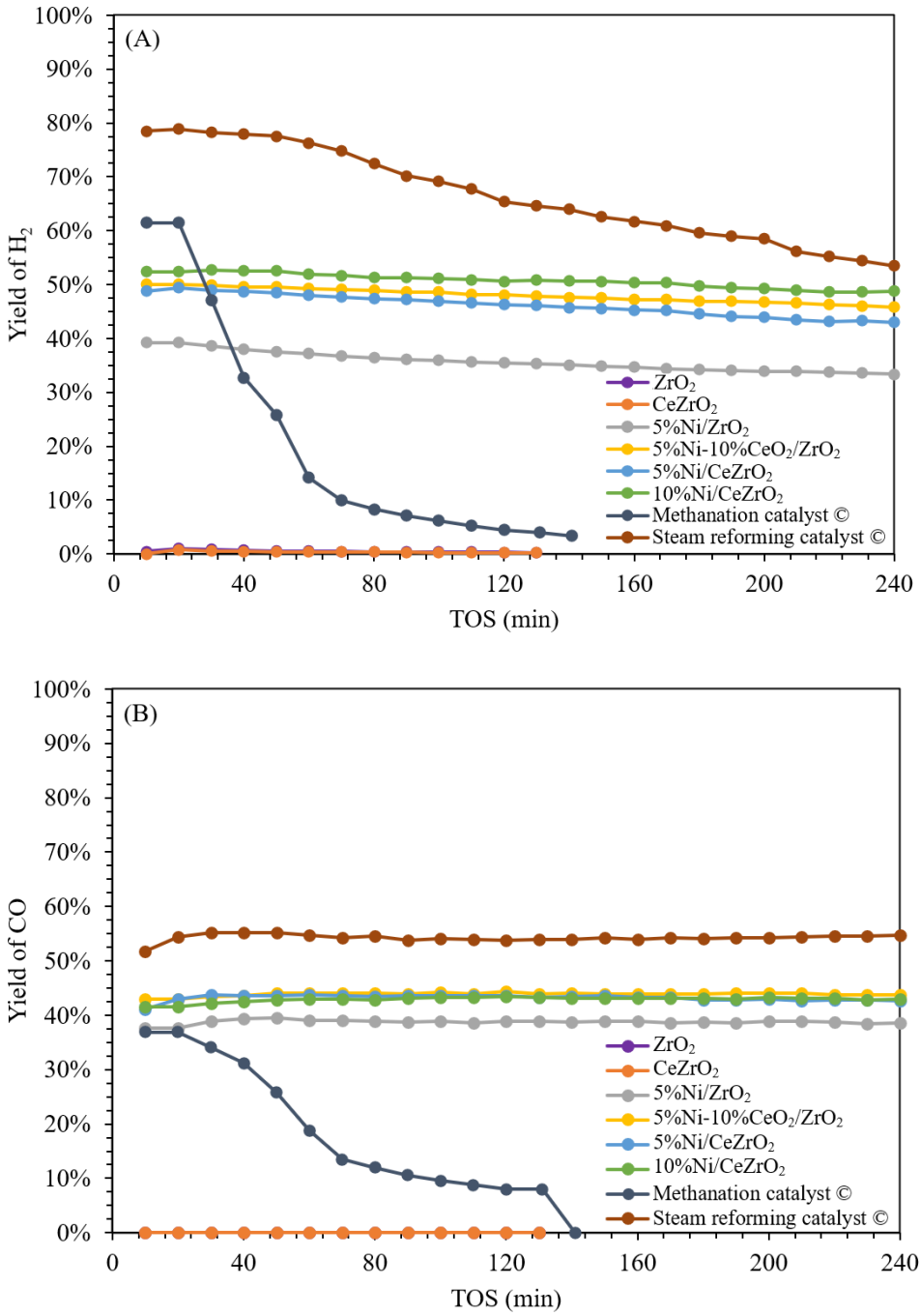

Figure 7. Yield of product on a ceria-zirconia-supported nickel catalyst: (**A**) H_2 and (**B**) CO (temperature of 700 °C, atmospheric pressure, WHSV 60,000 mL g^{-1} h^{-1}).

Among the catalysts evaluated in this study, the synthesized catalysts exhibit better catalytic performance when compared with the commercial catalysts in terms of the conversion of reactants per mass of the active Ni in the catalyst, which is 2.2 times higher for the 10%Ni/$CeZrO_2$ catalyst than for the commercial steam reforming catalyst. In addition, based on the H_2:CO product ratios shown in Figure 8, the 10%Ni/$CeZrO_2$ catalyst achieves the highest yields, with an H_2/CO ratio of ca. 1.4, whereas the thermodynamic ratio is ca. 1.5. The 5%Ni/$CeZrO_2$ and 5%Ni-10%CeO_2/$CeZrO_2$ catalysts achieve H_2:CO ratios of ca. 1.2. Meanwhile, for the catalysts that do not contain CeO_2, the H_2/CO ratio is ca. 1, which is lower in comparison.

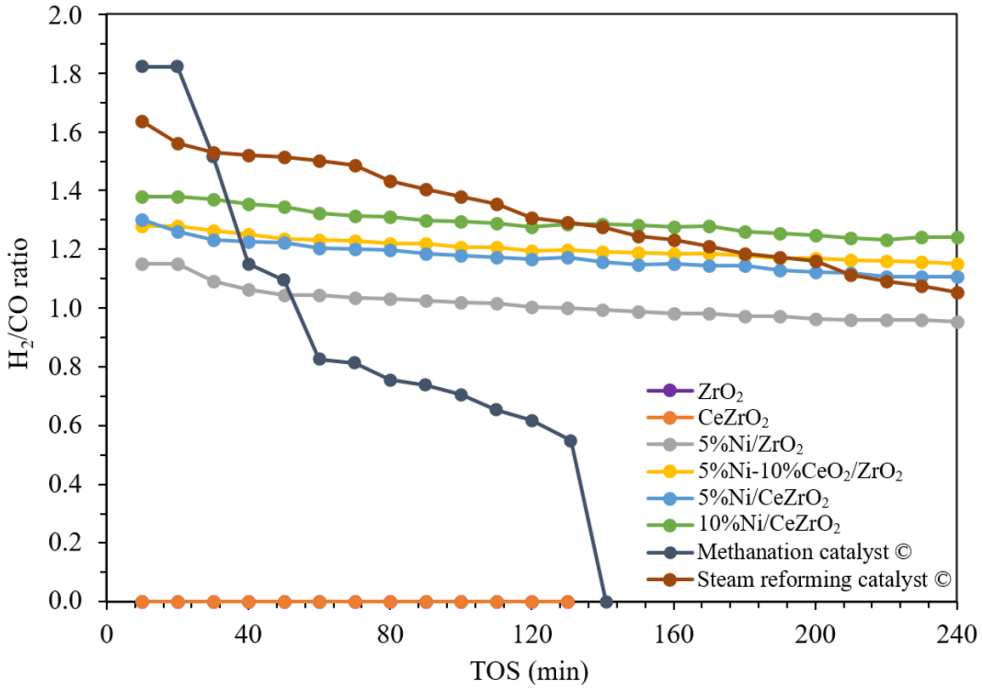

Figure 8. Ratio of H_2/CO on a ceria-zirconia-supported nickel catalyst (temperature of 700 °C, atmospheric pressure, WHSV 60,000 mL g^{-1} h^{-1}).

Overall, the synthesized catalysts have a more stable yield than the commercial catalysts. At the beginning of the experiment, the commercial steam reforming catalyst has a H_2:CO ratio of ca. 1.6, which decreases throughout the experiment to 1. Meanwhile, for the commercial methanation catalyst, the decrease in the H_2/CO ratio was more significant, starting from 1.8 and decreasing to 0.6 during the course of the experiment. The average H_2:CO ratios for the commercial steam reforming and methanation catalysts over the 240-min duration were ca. 1.3 and 0.6, respectively. The decrease in the H_2:CO ratio is caused by carbon deposition, which deactivates the catalyst. Meanwhile, the 10%Ni/$CeZrO_2$, 5%Ni/$CeZrO_2$, and 5%Ni-10%CeO_2/ZrO_2 catalysts have CeO_2 components that help minimize the coking process over the catalysts [40].

3.3. Carbon Formation in the Spent Catalyst

TGA was used to measure the carbon deposited on each catalyst after the 240-min stability evaluation at a temperature of 700 °C and atmospheric pressure. This method is based on the reduction in the sample mass, which took place under a flow of air as the temperature increases. The mass reduction of the sample occurs because of the evaporation of water and combustion of the carbon in the sample to produce CO_2.

The TGA profiles obtained for the catalysts evaluated in the DRM (Figure 9) show that the commercial steam reforming and methanation catalysts experience a higher reduction in sample mass due to the combustion of the carbon that was deposited during the catalyst performance evaluation when compared with the synthesized catalysts.

Figure 9 shows the mass reduction profiles of the synthesized and commercial steam reforming catalysts used for 240 min, as well as the profile for the commercial methanation catalyst that was only used for 140 min because the catalyst underwent deactivation. From the profiles, it can be seen that the masses of the synthesized catalysts do not experience a significant reduction when compared with that experienced by the commercial catalysts. The commercial steam reforming and methanation catalysts experience a mass reduction between 600 and 800 °C, which indicates the combustion of the previously deposited carbon on the catalyst. The amounts of carbon deposited on the catalysts are shown in Figure 10.

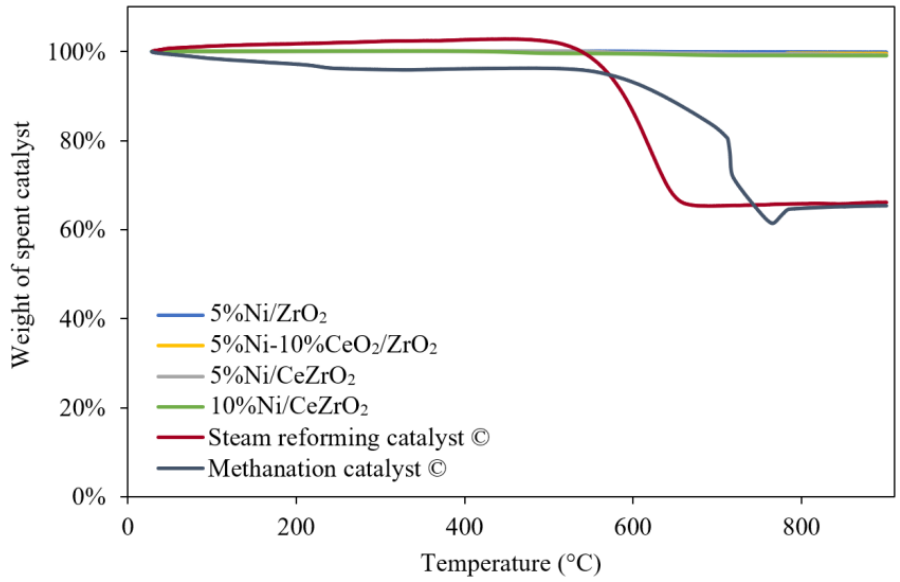

Figure 9. TGA patterns for spent catalyst.

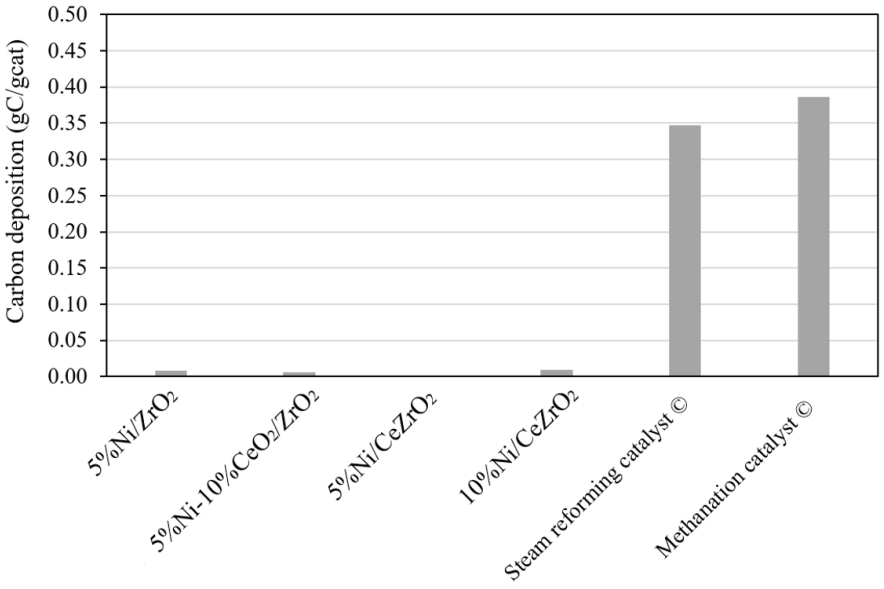

Figure 10. Carbon deposition of spent catalyst during activity and stability test.

It can be seen that the amounts of carbon present in the commercial catalysts are much higher than those in the synthesized catalysts. The amount of carbon deposited on the commercial steam reforming catalyst is 0.347 gC/gcat after the stability evaluation during the DRM over 240 min. Meanwhile, on the commercial methanation catalyst, the amount of carbon deposited is 0.386 gC/gcat after the stability evaluation during DRM over 140 min. The amounts of carbon in the commercial catalysts are probably caused by the sintering of Ni and Al_2O_3, which causes the aggregation of Ni particles, resulting in enhanced carbon deposition on the catalyst [60]. The higher the amount of Ni in the catalyst, the more carbon is deposited on the catalyst. A large amount of Ni in the commercial steam reforming catalyst (25 wt.%) also reduces Ni dispersion, thereby increasing the chances of sintering [61]. To confirm the occurrence of sintering in the commercial catalysts, further analyses, such as high-resolution transmission electron microscopy, XRD, and/or N_2 physisorption, are necessary.

The amounts of carbon deposited after the 240-min stability evaluation on the 10%Ni/$CeZrO_2$, 5%Ni/$CeZrO_2$, 5%Ni/ZrO_2, and 5%Ni-10%CeO_2/ZrO_2 are ca. 0.001 gC/gcat,

0.009 gC/gcat, 0.008 gC/gcat, and 0.006 gC/gcat, respectively. Due to the small amounts of carbon deposited on the synthesized catalysts, carbon deposition on these catalysts can be neglected. The higher stability of the synthesized catalysts when compared with the commercial catalysts is probably due to the catalyst components CeO_2 and ZrO_2. The chemical composition of the catalyst with a ceria-zirconia component has a strong influence on the relative contribution of CH_4 or the CO_2 activation pathway to carbon formation, as well as on the reactivity of carbon with oxygen species [62].

The vacant oxygen sites on the DRM catalyst provide sites for CO_2 activation and the breakdown of C-O bonds, thereby reducing the chance of catalyst deactivating due to carbon accumulation. This is because the lattice oxygens on the catalyst can oxidize the carbon to CO [15].

4. Conclusions

The performance of the ceria-zirconia-supported Ni catalysts in the DRM was evaluated based on the effect of the addition of ceria, catalyst preparation method, and Ni content on the physicochemical characteristics, performance, and stability of the resultant catalysts. The results of the BET analysis showed that the addition of 10 wt.% of ceria to ZrO_2 via co-precipitation to form $Ce_{0.1}Zr_{0.9}O_2$ ($CeZrO_2$) can increase the surface area by ca. 30%. As more NiO was impregnated into the support, the surface area of the catalyst decreased and the pore diameter increased. The H_2-TPR results showed that the 10%NiO/$CeZrO_2$ catalyst had a more intense peak for NiO reduction at a lower temperature when compared with those of the other synthesized catalysts. This is due to the higher amount of NiO and the shift of the reduction peak to a lower temperature caused by the H_2 spillover effect. Furthermore, this is buffered with the good redox properties of the support, which allow a more effective transfer of oxygen species. The results of the activity and stability evaluations of the catalysts at a temperature of 700 °C, pressure of 0.92 atm, and WHSV 60,000 mL g^{-1} h^{-1} showed that the 10%Ni/$CeZrO_2$ catalyst was the superior one, with a conversion of CH_4 and CO_2 of 74% and 55%, respectively. The H_2:CO ratio in the product was ca. 1.4, indicating a higher formation of H_2. The amounts of carbon deposited in the synthesized catalysts are minimal, i.e., <0.01 gC/gcat; therefore, the carbon deposition in the synthesized catalysts can be neglected. The use of CeO_2 and ZrO_2 in the DRM could help in minimizing coke formation due to the improved oxygen storage and mobility.

Author Contributions: Conceptualization, I.C.S., F.I., H.D., N.N. and Y.W.B.; methodology, I.C.S.; software, I.C.S.; validation, I.C.S. and Y.W.B.; formal analysis, I.C.S., F.I., H.D. and N.N.; investigation, I.C.S.; data curation, I.C.S., F.I., H.D. and Y.W.B.; writing—original draft preparation, I.C.S.; writing—review and editing, I.C.S., F.I., H.D., N.N. and Y.W.B.; visualization, I.C.S.; supervision, Y.W.B. and N.N.; project administration, Y.W.B.; funding acquisition, Y.W.B. All authors have read and agreed to the published version of the manuscript.

Funding: The Indonesia Endowment Fund for Education (LPDP), Indonesian Science Fund (DIPI), and the Ministry of Finance of Indonesia [grant number: RISPRO/KI/BI/KOM/II/16507/I/2020].

Institutional Review Board Statement: Not applicable.

Informed Consent Statement: Not applicable.

Data Availability Statement: The data presented in this study are available on request from the corresponding author.

Conflicts of Interest: The authors declare no conflict of interest.

References

1. Budhi, Y.W.; Effendy, M.; Bindar, Y. Subagjo Dynamic Behavior of Reverse Flow Reactor for Lean Methane Combustion. *J. Eng. Technol. Sci.* **2014**, *46*, 299–317. [CrossRef]
2. Riemer, P. Greenhouse Gas Mitigation Technologies, an Overview of the C02 Capture, Storage and Future Activities of the IEA Greenhouse Gas R&D Programme. *Energy Convers. Manag.* **1996**, *37*, 665–670.

3. Lavoie, J.M. Review on Dry Reforming of Methane, a Potentially More Environmentally-Friendly Approach to the Increasing Natural Gas Exploitation. *Front. Chem.* **2014**, *2*, 81. [CrossRef]
4. Zhang, G.; Liu, J.; Xu, Y.; Sun, Y. A Review of CH_4–CO_2 Reforming to Synthesis Gas over Ni-Based Catalysts in Recent Years (2010–2017). *Int. J. Hydrogen Energy* **2018**, *43*, 15030–15054. [CrossRef]
5. Usman, M.; Wan Daud, W.M.A.; Abbas, H.F. Dry Reforming of Methane: Influence of Process Parameters–A Review. *Renew. Sustain. Energy Rev.* **2015**, *45*, 710–744. [CrossRef]
6. Jang, W.J.; Shim, J.O.; Kim, H.M.; Yoo, S.Y.; Roh, H.S. A Review on Dry Reforming of Methane in Aspect of Catalytic Properties. *Catal. Today* **2019**, *324*, 15–26. [CrossRef]
7. Wang, Y.; Fang, Q.; Shen, W.; Zhu, Z.; Fang, Y. ($Ni/MgAl_2O_4$)@SiO_2 Core–Shell Catalyst with High Coke-Resistance for the Dry Reforming of Methane. *React. Kinet. Mech. Catal.* **2018**, *125*, 127–139. [CrossRef]
8. Das, S.; Pérez-Ramírez, J.; Gong, J.; Dewangan, N.; Hidajat, K.; Gates, B.C.; Kawi, S. Core-Shell Structured Catalysts for Thermocatalytic, Photocatalytic, and Electrocatalytic Conversion of CO_2. *Chem. Soc. Rev.* **2020**, *49*, 2937–3004. [CrossRef]
9. Hoseinzade, L.; Adams, T.A. Dynamic Modeling of Integrated Mixed Reforming and Carbonless Heat Systems. *Ind. Eng. Chem. Res.* **2018**, *57*, 6013–6023. [CrossRef]
10. Balasubramanian, P.; Bajaj, I.; Hasan, M.M.F. Simulation and Optimization of Reforming Reactors for Carbon Dioxide Utilization Using Both Rigorous and Reduced Models. *J. CO_2 Util.* **2018**, *23*, 80–104. [CrossRef]
11. Mahboob, S.; Haghighi, M.; Rahmani, F. Sonochemically Preparation and Characterization of Bimetallic Ni-Co/Al_2O_3-ZrO_2 Nanocatalyst: Effects of Ultrasound Irradiation Time and Power on Catalytic Properties and Activity in Dry Reforming of CH_4. *Ultrason. Sonochem.* **2017**, *38*, 38–49. [CrossRef] [PubMed]
12. Wang, Y.; Yao, L.; Wang, Y.; Wang, S.; Zhao, Q.; Mao, D.; Hu, C. Low-Temperature Catalytic CO_2 Dry Reforming of Methane on Ni-Si/ZrO_2 Catalyst. *ACS Catal.* **2018**, *8*, 6495–6506. [CrossRef]
13. Baena-Moreno, F.M.; Rodríguez-Galán, M.; Vega, F.; Alonso-Fariñas, B.; Vilches Arenas, L.F.; Navarrete, B. Carbon Capture and Utilization Technologies: A Literature Review and Recent Advances. *Energy Sour. Part A Recovery Util. Environ. Eff.* **2019**, *41*, 1403–1433. [CrossRef]
14. Kathiraser, Y.; Oemar, U.; Saw, E.T.; Li, Z.; Kawi, S. Kinetic and Mechanistic Aspects for CO_2 Reforming of Methane over Ni Based Catalysts. *Chem. Eng. J.* **2015**, *278*, 62–78. [CrossRef]
15. Pakhare, D.; Spivey, J. A Review of Dry (CO_2) Reforming of Methane over Noble Metal Catalysts. *Chem. Soc. Rev.* **2014**, *43*, 7813–7837. [CrossRef] [PubMed]
16. Khani, Y.; Shariatinia, Z.; Bahadoran, F. High Catalytic Activity and Stability of $ZnLaAlO_4$ Supported Ni, Pt and Ru Nanocatalysts Applied in the Dry, Steam and Combined Dry-Steam Reforming of Methane. *Chem. Eng. J.* **2016**, *299*, 353–366. [CrossRef]
17. Oliveira, A.C.; Carvalho, D.C.; de Souza, H.S.A.; Filho, J.M.; Oliveira, A.C.; Campos, A.; Milet, É.R.C.; de Sousa, F.F.; Padron-Hernandez, E. A Study on the Modification of Mesoporous Mixed Oxides Supports for Dry Reforming of Methane by Pt or Ru. *Appl. Catal. A Gen.* **2014**, *473*, 132–145. [CrossRef]
18. Wang, F.; Xu, L.; Shi, W.; Zhang, J.; Wu, K.; Zhao, Y.; Li, H.; Li, H.X.; Xu, G.Q.; Chen, W. Thermally Stable Ir/$Ce_{0.9}La_{0.1}O_2$ Catalyst for High Temperature Methane Dry Reforming Reaction. *Nano Res.* **2017**, *10*, 364–380. [CrossRef]
19. Li, L.; Zhou, L.; Ould-Chikh, S.; Anjum, D.H.; Kanoun, M.B.; Scaranto, J.; Hedhili, M.N.; Khalid, S.; Laveille, P.V.; D'Souza, L.; et al. Controlled Surface Segregation Leads to Efficient Coke-Resistant Nickel/Platinum Bimetallic Catalysts for the Dry Reforming of Methane. *ChemCatChem* **2015**, *7*, 819–829. [CrossRef]
20. Yentekakis, I.V.; Goula, G.; Panagiotopoulou, P.; Katsoni, A.; Diamadopoulos, E.; Mantzavinos, D.; Delimitis, A. Dry Reforming of Methane: Catalytic Performance and Stability of Ir Catalysts Supported on γ-Al_2O_3, $Zr_{0.92}Y_{0.08}O_{2-\delta}$ (YSZ) or $Ce_{0.9}Gd_{0.1}O_{2-\delta}$ (GDC) Supports. *Top. Catal.* **2015**, *58*, 1228–1241. [CrossRef]
21. Singh, S.A.; Madras, G. Sonochemical Synthesis of Pt, Ru Doped TiO_2 for Methane Reforming. *Appl. Catal. A Gen.* **2016**, *518*, 102–114. [CrossRef]
22. Pakhare, D.; Shaw, C.; Haynes, D.; Shekhawat, D.; Spivey, J. Effect of Reaction Temperature on Activity of Pt- and Ru-Substituted Lanthanum Zirconate Pyrochlores ($La_2Zr_2O_7$) for Dry (CO_2) Reforming of Methane (DRM). *J. CO_2 Util.* **2013**, *1*, 37–42. [CrossRef]
23. Jabbour, K.; el Hassan, N.; Casale, S.; Estephane, J.; el Zakhem, H. Promotional Effect of Ru on the Activity and Stability of Co/SBA-15 Catalysts in Dry Reforming of Methane. *Int. J. Hydrogen Energy* **2014**, *39*, 7780–7787. [CrossRef]
24. Kamieniak, J.; Bernalte, E.; Doyle, A.M.; Kelly, P.J.; Banks, C.E. Can Ultrasound or PH Influence Pd Distribution on the Surface of HAP to Improve Its Catalytic Properties in the Dry Reforming of Methane? *Catal. Lett.* **2017**, *147*, 2200–2208. [CrossRef]
25. Singha, R.K.; Yadav, A.; Shukla, A.; Kumar, M.; Bal, R. Low Temperature Dry Reforming of Methane over Pd-CeO_2 Nanocatalyst. *Catal. Commun.* **2017**, *92*, 19–22. [CrossRef]
26. Pizzolitto, C.; Pupulin, E.; Menegazzo, F.; Ghedini, E.; di Michele, A.; Mattarelli, M.; Cruciani, G.; Signoretto, M. Nickel Based Catalysts for Methane Dry Reforming: Effect of Supports on Catalytic Activity and Stability. *Int. J. Hydrogen Energy* **2019**, *44*, 28065–28076. [CrossRef]
27. Dekkar, S.; Tezkratt, S.; Sellam, D.; Ikkour, K.; Parkhomenko, K.; Martinez-Martin, A.; Roger, A.C. Dry Reforming of Methane over Ni–Al_2O_3 and Ni–SiO_2 Catalysts: Role of Preparation Methods. *Catal. Lett.* **2020**, *150*, 2180–2199. [CrossRef]
28. Chen, W.; Zhao, G.; Xue, Q.; Chen, L.; Lu, Y. High Carbon-Resistance Ni/$CeAlO_3$-Al_2O_3 Catalyst for CH_4/CO_2 Reforming. *Appl. Catal. B Environ.* **2013**, *136–137*, 260–268. [CrossRef]

29. Zeng, S.; Zhang, L.; Zhang, X.; Wang, Y.; Pan, H.; Su, H. Modification Effect of Natural Mixed Rare Earths on Co/γ-Al_2O_3 Catalysts for CH_4/CO_2 Reforming to Synthesis Gas. *Int. J. Hydrogen Energy* **2012**, *37*, 9994–10001. [CrossRef]
30. Wang, F.; Xu, L.; Shi, W. Syngas Production from CO_2 Reforming with Methane over Core-Shell Ni@SiO_2 Catalysts. *J. CO_2 Util.* **2016**, *16*, 318–327. [CrossRef]
31. Baktash, E.; Littlewood, P.; Schomäcker, R.; Thomas, A.; Stair, P.C. Alumina Coated Nickel Nanoparticles as a Highly Active Catalyst for Dry Reforming of Methane. *Appl. Catal. B Environ.* **2015**, *179*, 122–127. [CrossRef]
32. Gao, X.; Tan, Z.; Hidajat, K.; Kawi, S. Highly Reactive Ni-Co/SiO_2 Bimetallic Catalyst via Complexation with Oleylamine/Oleic Acid Organic Pair for Dry Reforming of Methane. *Catal. Today* **2017**, *281*, 250–258. [CrossRef]
33. Xu, J.; Xiao, Q.; Zhang, J.; Sun, Y.; Zhu, Y. NiO-MgO Nanoparticles Confined inside SiO_2 Frameworks to Achieve Highly Catalytic Performance for CO_2 Reforming of Methane. *Mol. Catal.* **2017**, *432*, 31–36. [CrossRef]
34. Zhang, L.; Wang, X.; Chen, C.; Zou, X.; Ding, W.; Lu, X. Dry Reforming of Methane to Syngas over Lanthanum-Modified Mesoporous Nickel Aluminate/Γ-Alumina Nanocomposites by One-Pot Synthesis. *Int. J. Hydrogen Energy* **2017**, *42*, 11333–11345. [CrossRef]
35. Ghods, B.; Meshkani, F.; Rezaei, M. Effects of Alkaline Earth Promoters on the Catalytic Performance of the Nickel Catalysts Supported on High Surface Area Mesoporous Magnesium Silicate in Dry Reforming Reaction. *Int. J. Hydrogen Energy* **2016**, *41*, 22913–22921. [CrossRef]
36. Titus, J.; Roussière, T.; Wasserschaff, G.; Schunk, S.; Milanov, A.; Schwab, E.; Wagner, G.; Oeckler, O.; Gläser, R. Dry Reforming of Methane with Carbon Dioxide over NiO-MgO-ZrO_2. *Catal. Today* **2016**, *270*, 68–75. [CrossRef]
37. Budiman, A.W.; Song, S.H.; Chang, T.S.; Shin, C.H.; Choi, M.J. Dry Reforming of Methane Over Cobalt Catalysts: A Literature Review of Catalyst Development. *Catal. Surv. Asia* **2012**, *16*, 183–197. [CrossRef]
38. Alipour, Z.; Rezaei, M.; Meshkani, F. Effect of Ni Loadings on the Activity and Coke Formation of MgO-Modified Ni/Al_2O_3 Nanocatalyst in Dry Reforming of Methane. *J. Energy Chem.* **2014**, *23*, 633–638. [CrossRef]
39. Faria, E.C.; Neto, R.C.R.; Colman, R.C.; Noronha, F.B. Hydrogen Production through CO_2 Reforming of Methane over Ni/$CeZrO_2$/Al_2O_3 Catalysts. *Catal. Today* **2014**, *228*, 138–144. [CrossRef]
40. Teh, L.P.; Setiabudi, H.D.; Timmiati, S.N.; Aziz, M.A.A.; Annuar, N.H.R.; Ruslan, N.N. Recent Progress in Ceria-Based Catalysts for the Dry Reforming of Methane: A Review. *Chem. Eng. Sci.* **2021**, *242*, 116606. [CrossRef]
41. Damyanova, S.; Pawelec, B.; Arishtirova, K.; Huerta, M.V.M.; Fierro, J.L.G. The Effect of CeO_2 on the Surface and Catalytic Properties of Pt/CeO_2-ZrO_2 Catalysts for Methane Dry Reforming. *Appl. Catal. B Environ.* **2009**, *89*, 149–159. [CrossRef]
42. Singha, R.K.; Das, S.; Pandey, M.; Kumar, S.; Bal, R.; Bordoloi, A. Ni Nanocluster on Modified CeO_2-ZrO_2 Nanoporous Composite for Tri-Reforming of Methane. *Catal. Sci. Technol.* **2016**, *6*, 7122–7136. [CrossRef]
43. Wolfbeisser, A.; Sophiphun, O.; Bernardi, J.; Wittayakun, J.; Föttinger, K.; Rupprechter, G. Methane Dry Reforming over Ceria-Zirconia Supported Ni Catalysts. *Catal. Today* **2016**, *277*, 234–245. [CrossRef]
44. Muñoz, M.A.; Calvino, J.J.; Rodríguez-Izquierdo, J.M.; Blanco, G.; Arias, D.C.; Pérez-Omil, J.A.; Hernández-Garrido, J.C.; González-Leal, J.M.; Cauqui, M.A.; Yeste, M.P. Highly Stable Ceria-Zirconia-Yttria Supported Ni Catalysts for Syngas Production by CO_2 Reforming of Methane. *Appl. Surf. Sci.* **2017**, *426*, 864–873. [CrossRef]
45. Mesrar, F.; Kacimi, M.; Liotta, L.F.; Puleo, F.; Ziyad, M. Syngas Production from Dry Reforming of Methane over Ni/Perlite Catalysts: Effect of Zirconia and Ceria Impregnation. *Int. J. Hydrogen Energy* **2018**, *43*, 17142–17155. [CrossRef]
46. Paladino Lino, A.V.; Rodella, C.B.; Assaf, E.M.; Assaf, J.M. Methane Tri-Reforming for Synthesis Gas Production Using Ni/$CeZrO_2$/$MgAl_2O_4$ Catalysts: Effect of Zr/Ce Molar Ratio. *Int. J. Hydrogen Energy* **2020**, *45*, 8418–8432. [CrossRef]
47. Zhang, F.; Liu, Z.; Chen, X.; Rui, N.; Betancourt, L.E.; Lin, L.; Xu, W.; Sun, C.J.; Abeykoon, A.M.M.; Rodriguez, J.A.; et al. Effects of Zr Doping into Ceria for the Dry Reforming of Methane over Ni/$CeZrO_2$ Catalysts: In Situ Studies with XRD, XAFS, and AP-XPS. *ACS Catal.* **2020**, *10*, 3274–3284. [CrossRef]
48. Kambolis, A.; Matralis, H.; Trovarelli, A.; Papadopoulou, C. Ni/CeO_2-ZrO_2 Catalysts for the Dry Reforming of Methane. *Appl. Catal. A Gen.* **2010**, *377*, 16–26. [CrossRef]
49. Kumar, P.; Sun, Y.; Idem, R.O. Nickel-Based Ceria, Zirconia, and Ceria-Zirconia Catalytic Systems for Low-Temperature Carbon Dioxide Reforming of Methane. *Energy Fuels* **2007**, *21*, 3113–3123. [CrossRef]
50. Basahel, S.N.; Ali, T.T.; Mokhtar, M.; Narasimharao, K. Influence of Crystal Structure of Nanosized ZrO_2 on Photocatalytic Degradation of Methyl Orange. *Nanoscale Res. Lett.* **2015**, *10*, 73. [CrossRef]
51. Sophiana, I.C.; Topandi, A.; Iskandar, F.; Devianto, H.; Nishiyama, N.; Budhi, Y.W. Catalytic Oxidation of Benzene at Low Temperature over Novel Combination of Metal Oxide Based Catalysts: CuO, MnO_2, NiO with $Ce_{0.75}Zr_{0.25}O_2$ as Support. *Mater. Today Chem.* **2020**, *17*, 100305. [CrossRef]
52. Deng, Q.F.; Ren, T.Z.; Agula, B.; Liu, Y.; Yuan, Z.Y. Mesoporous CexZr1-XO_2 Solid Solutions Supported CuO Nanocatalysts for Toluene Total Oxidation. *J. Ind. Eng. Chem.* **2014**, *20*, 3303–3312. [CrossRef]
53. Pham, P.T.M.; le Minh, T.; Nguyen, T.T.; van Driessche, I. Ceo_2 Based Catalysts for the Treatment of Propylene in Motorcycle's Exhaust Gases. *Materials* **2014**, *7*, 7379–7397. [CrossRef]
54. Argyle, M.D.; Bartholomew, C.H. Heterogeneous Catalyst Deactivation and Regeneration: A Review. *Catalysts* **2015**, *5*, 145–269. [CrossRef]
55. Vagia, E.C.; Lemonidou, A.A. Hydrogen Production via Steam Reforming of Bio-Oil Components over Calcium Aluminate Supported Nickel and Noble Metal Catalysts. *Appl. Catal. A Gen.* **2008**, *351*, 111–121. [CrossRef]

56. Ibrahim, A.A.; Al-Fatesh, A.A.; Atia, H.; Fakeeha, A.H.; Kasim, S.O.; Abasaeed, A.E. Influence of Promoted 5%Ni/MCM-41 Catalysts on Hydrogen Yield in CO_2 Reforming of CH_4. *Int. J. Energy Res.* **2018**, *42*, 4120–4130. [CrossRef]
57. Tan, M.; Wang, X.; Hu, Y.; Shang, X.; Zhang, L.; Zou, X.; Ding, W.; Lu, X. Influence of Nickel Content on Structural and Surface Properties, Reducibility and Catalytic Behavior of Mesoporous γ-Alumina-Supported Ni-Mg Oxides for Pre-Reforming of Liquefied Petroleum Gas. *Catal. Sci. Technol.* **2016**, *6*, 3049–3063. [CrossRef]
58. Wang, Y.; Yao, L.; Wang, S.; Mao, D.; Hu, C. Low-Temperature Catalytic CO_2 Dry Reforming of Methane on Ni-Based Catalysts: A Review. *Fuel Process. Technol.* **2018**, *169*, 199–206. [CrossRef]
59. Nguyen-Huy, C.; Shin, E.W. Oxidative Cracking of Vacuum Residue with Steam over NiK/CeZr–Al Catalysts. *Fuel* **2017**, *192*, 149–157. [CrossRef]
60. Jabbour, K.; Massiani, P.; Davidson, A.; Casale, S.; el Hassan, N. Ordered Mesoporous "One-Pot" Synthesized Ni-Mg(Ca)-Al_2O_3 as Effective and Remarkably Stable Catalysts for Combined Steam and Dry Reforming of Methane (CSDRM). *Appl. Catal. B Environ.* **2017**, *201*, 527–542. [CrossRef]
61. Rahbar Shamskar, F.; Rezaei, M.; Meshkani, F. The Influence of Ni Loading on the Activity and Coke Formation of Ultrasound-Assisted Co-Precipitated Ni–Al_2O_3 Nanocatalyst in Dry Reforming of Methane. *Int. J. Hydrogen Energy* **2017**, *42*, 4155–4164. [CrossRef]
62. Makri, M.M.; Vasiliades, M.A.; Petallidou, K.C.; Efstathiou, A.M. Effect of Support Composition on the Origin and Reactivity of Carbon Formed during Dry Reforming of Methane over 5 wt% Ni/$Ce_{1-X}M_xO_{2-\delta}$ (M = Zr^{4+}, Pr^{3+}) Catalysts. *Catal. Today* **2016**, *259*, 150–164. [CrossRef]